EPJ manuscript No.
(will be inserted by the editor)

Moment Analysis and Zipf Law

Y.G. Ma[1]

Shanghai Institute of Applied Physics, Chinese Academy of Sciences, Shanghai 201800, China

Received: date / Revised version: date

Abstract. Moment analysis method and nuclear Zipf's law of fragment size distributions have been proposed for the studies of the nuclear disassembly and liquid gas phase transition. In this report, we present a compilation of both theoretical and experimental studies on moment analysis and Zipf law performed so far. The relationship of both methods to the critical behavior of nuclear disassembly has been discussed. In addition, scaled factorial moment and intermittency are also simply review.

PACS. PACS-key discribing text of that key – PACS-key discribing text of that key

1 Introduction

Hot nuclei can be formed in energetic heavy ion collisions (HIC) and deexcite by different decay modes, such as evaporation and multifragmentation. Experimentally, this kind of multifragment emission was observed to evolve with excitation energy. Multiplicity, N_{imf}, of intermediate mass fragment (IMF) rises with the beam energy, reaches a maximum, and finally falls to lower value. This phenomenon of the rise and fall of N_{imf} may be related to the liquid gas phase transition in nuclear matter [1]. The onset of multifragmentation probably indicates the coexistence of liquid and gas phases. The mass (charge) distribution of IMF distribution can be expressed as power law with parameter τ. The minimum of τ, τ_{min}, occurs when the liquid gas phase transition takes place [2].

On the other hand, the caloric curve measurement can also provide useful information on the liquid gas phase transition [3–7]. The analysis of critical exponents provides additional judgements of the critical behavior of finite nuclear system [8–13]. More observables are suggested to judge the liquid gas phase transition of nuclei [14–19]. Some reviews can be found in this book [20–25].

In this report, we will review the moment analysis method and Zipf law of fragment size distribution. The phenomenological base of moment analysis is introduced in the Sec. 2. The finite size effect is discussed in Sec.3. Sec. 4 gives the application of moment analysis in multifragmention and its relation to the critical behavior. Scaled factorial moments and intermittency is discussed in Sec. 5. In Sec. 6 Zipf law is introduced into nuclear fragment distribution and the corresponding simulations are given; The experimental evidences of nuclear Zipf law are also presented in Sec. 7; Finally the summary is given in Sec. 8.

Send offprint requests to:

2 Phenomenological Base of Moment Analysis

Campi [26,27] and Bauer [28,29] *et al.* first suggested that the methods used in percolation studies may be applied to nuclear multifragmentation data. In percolation theory the moments of the cluster distribution contain the signature of critical behavior [30]. The method of moment analysis has been experimentally used to search for evidence of the liquid-gas phase transition in multifragmentation. The definition of the k moments of the cluster size distribution is

$$M_k(n) = \sum_{A \neq A_{max}} A^k n_A(m), \tag{1}$$

where A is fragment mass and $n_A(m)$ is its multiplicity. The sum runs over all masses A in the event including neutrons except for the heaviest fragment (A_{max}). This quantity was taken as a basic tool in extracting the critical exponents in Au + C data [9]. It has been argued that there should be an enhancement in the critical region of the moment, M_k, for $k > \tau - 1$, with critical exponent $\tau > 2$ [26,27].

In experimental analysis, events are sorted by different condition. In this case, so-called conditional moment is used to describe the fragment distribution. Usually mean value of M_k for events with given M'_k, eg. M_2 for events with given multiplicity M_0, Z_{bound} etc, is called conditional moment. Fig. 1 shows that $m_2(n)$, M_2 divided by the lattice sites S_0, is the same for nuclear data points (full circles) as given by percolation model where a sharp second order phase transition is expected (open circles) but is qualitatively different from a linear chain model with S_0 lattices site where we can never have a phase transition. The maximum of m_2 at $n \sim 0.25$ (n is the multiplicity divided by the S_0) is the manifestation of a phase transi-

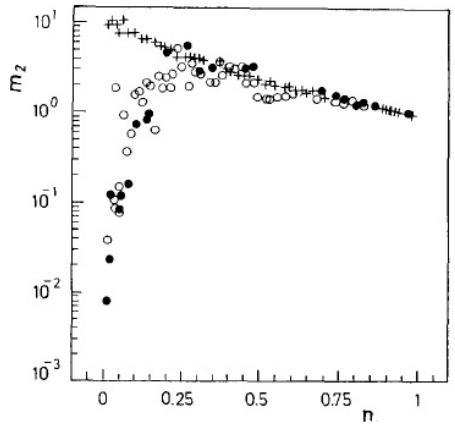

Fig. 1. The conditional moments m_2(n) for model (a): one-dimensional model (crosses); model (b): three dimensional percolation model (open circles); and model (c): experimental gold fragmentation (full circles), as a function of the reduced multiplicity n. Figure is taken from Ref. [27].

tion. The broad maximum instead of a singularity is due to the finite size of the system.

More insight in the shape of the fragment size distribution is obtained by looking at a combination of moments M_k. For example, the quantity

$$\gamma_2 = \frac{M_2 M_0}{M_1^2} = \frac{\sigma^2}{\langle s \rangle^2} + 1, \tag{2}$$

where $M_1$and M_2 are the first and second moments of the mass distribution in an event and M_0 is the total multiplicity including neutrons. σ^2 is the variance of fragment distribution and $\langle s \rangle = M_1/M_0$ represents the mean fragment size. γ_2 takes the value $\gamma_2 = 2$ for a pure exponential distribution $N(s) \sim exp(-\alpha s)$ regardless the value of α, but $\gamma_2 \gg 2$ for a power-law distribution $N(s) \sim s^{-\tau}$ when $\tau > 2$. In percolation model, the position of the maximum γ_2 value defines the critical point, where the fluctuation in the fragment size distribution are the largest. Usually the critical behavior requires that the peak value of γ_2 be larger than 2 [26,27]. However, this is not always true when the system size decreases due to the finite size effect, as we can see in the following sections.

Campi also suggested to use the single event (j) moment, i.e.

$$M_k^{(j)} = \sum_{A \neq A_{max}} A^k n^{(j)} \tag{3}$$

to investigate the shape of fragment size distribution. Also a normalized moments [26]

$$S_k^{(j)} = M_k^{(j)} / M_1^{(j)} \tag{4}$$

is defined. It was suggested the use of event by event scatter plots of the natural log of the size of the largest cluster, $\ln A_{max}$ or $\ln Z_{max}$ versus the natural log of the second moment, $\ln M_2$, or the normalized moment $\ln S_2$ to search for the largest fluctuation point. The examples will be given in following sections.

In percolation model with critical phenomenon, the cluster size distribution for infinite systems near critical regime can be expressed by

$$n(s) \sim s^{-\tau} f(\epsilon s^{\sigma}). \tag{5}$$

where s is the size of finite clusters, τ and σ two critical exponents and ϵ a variable that characterizes the state of the system. In thermal phase transitions $\epsilon = T - T_c$ is the distance to the critical temperature T_c. In percolation $\epsilon = p_c - p$ is the distance to the critical fraction of active bonds or occupied site p_c. The scaling function $f(\epsilon s^{\sigma})$ satisfies $f(0) = 1$, decaying rapidly (exponentially) for large values of $|\epsilon|$. In addition the theories predict that when $\epsilon < 0$ one infinite cluster (liquid or gel) is present in the system while no such cluster exists when $\epsilon > 0$ (only droplets or n-mers). In finite systems the same behavior is observed, especially when the largest cluster is also counted separately.

3 Finite Size Effect

Since the nucleus is a finite size system, the macroscopic thermal limit may not be applied. Therefore the finite size effect on phase transition behavior should be checked. In this section, we give some examples to illustrate this problem.

The percolation on a cubic lattice of linear size L containing L^3 sites, for $L = 4$ to 10, where all the sites are occupied and bonds are assumed to exist between neighbouring sites with bond probability p has been considered [31]. Sites that are connected together by such bonds are said to belong to the same cluster. It is well known that in such a model there exists a critical (or threshold) probability p_c such that for $p > p_c$ there is a large cluster that percolates throughout the lattice from end to end whereas for $p < p_c$ no such cluster exists and all the sites belong to small clusters (including isolated sites, i.e. singlet or clusters of size 1). As $L \to \infty$ the phase transition becomes sharper and smaller and p_c approaches a limiting value which for bond percolation on a cubic lattice is p_c = 0.249 [30]. For finite systems the threshold percolation probability is not so sharply defined.

In order to quantitatively illustrate the finite size effect on the critical behavior, the average of S_2 ($\overline{S_2}$) over all events belonging to the same value of $\ln P$ was calculated [31]. The results obtained by such averaging are presented by the dots shown in Fig. 2 for various cubic lattices with linear dimension L = 4 - 10 sites [31]. The location of the maximum value of $\overline{S_2}$ is now defined as corresponding to the location of the critical point which is a standard way of determining the percolation threshold [32]. The slope of the lower branches of the curves in Fig. 2 can also be calculated. This slope is expected to be $1 + \beta/\gamma$ which for percolation in three dimensions is equal to 1.25 when the values of the critical exponents of liquid gas universal class are used. For comparison the slopes of the straight

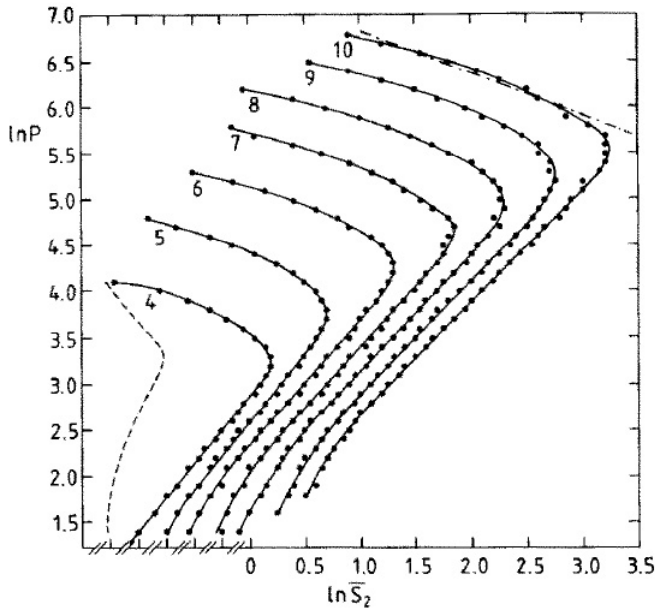

Fig. 2. The logarithm of the largest fragment size P as a function of the logarithm of the corresponding average second moment S_2 for bond percolation on simple cubic lattices of linear size ranging from L = 4 - 10 sites. The dots represent the actual calculation results and the curves drawn are just to guide the eye. The number next to each curve gives the value of the linear size L. Note that the lnS_2 scale given corresponds to the $L = 10$ curve. The other curves are successively shifted to the left with respect to each other by a distance of 0.25. The dashed curve and the dotted-dashed straight line are explained in the text. Figure is taken from Ref. [31].

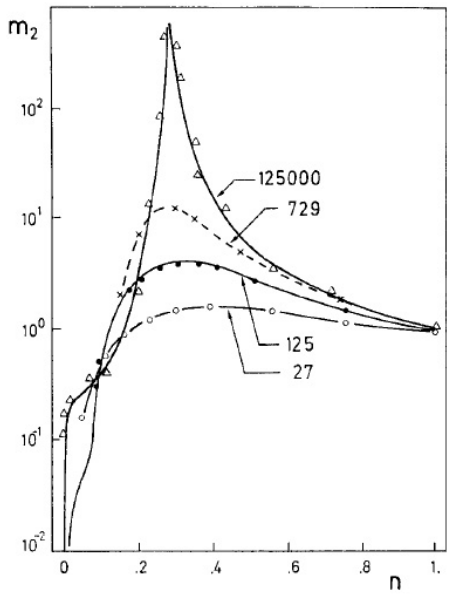

Fig. 3. The conditional moments $m_2(n)$ for percolation in a cubic lattice of linear size L = 3, 5, 9 and 50. Figure is taken from Ref. [27].

lines by a lest-squares fit to the lower branches of the L = 4 to 10 curves are found, in ascending order of L, to have the values 1.582±0.036, 1.503±0.029, 1.375±0.017, 1.355±0.021, 1.260±0.007, 1.258±0.014 and 1.242±0.015 [31]. This indicates that these slopes rapidly approach the value expected in the thermodynamic limit. In calculating these slopes we have excluded the points near the bottom of the branch in the region where the curves in Fig. 2 deviated noticeably from a straight line. These points correspond to events that are far from the critical region.

Similar to the analysis for the correlation of $\overline{S_2}$ and ln$P$, the finite size effect has been also investigated for m_2 by Campi [27]. This is shown in Fig. 3, where $m_2(n)$ is plotted for various system size ($50^3, 9^3, 5^3$ and 3^3) of the percolation model. We see clearly the critical behavior for the largest system and how it is smoothed when decreasing the size [27].

4 Moment analysis method and its application

Moment analysis method is useful to obtain some information about the critical behavior. In general, the critical exponents can be defined according to the standard procedure followed in condensed matter physics. For example,

$$M_k(\epsilon) = \sum_s = s^k n(s) \sim |\epsilon|^{\frac{\tau-k-1}{\sigma}}, (\epsilon \to 0) \qquad (6)$$

where τ and σ is the critical exponents. Since the exponent τ satisfies $2 < \tau < 3$, the second and high moments diverge at the critical point. In contrast the lower moments M_0 and M_1, which correspond to the number of fragments and the total mass, do not diverge.

In percolation scaling theory, there exists following relationship between the critical exponents and the moments:

$$\begin{aligned} M_0 &\sim |\epsilon|^{2-\alpha}, \\ M_1 &\sim |\epsilon|^{\beta}, \\ M_2 &\sim |\epsilon|^{-\gamma}, \end{aligned} \qquad (7)$$

where β and γ is other two critical exponents. A relationship between some critical exponents exists, namely

$$2\beta + \gamma = \frac{\tau - 1}{\sigma} = 2 - \alpha. \qquad (8)$$

In finite system the transitions are smooth but it is still possible to determine some critical exponents. By analogy with thermal phase transitions, one says that these moments exhibit a critical behavior. In Fisher model, thermal critical point is also a critical point for moments of the fragment size distribution.

In order to illustrate the application of moment analysis, we show the EOS data and NIMROD data as examples.

4.1 EOS data

4.1.1 Experimental description

The reverse kinematic EOS experiment was performed with 1 A GeV ^{197}Au, ^{139}La, and ^{84}Kr beams on carbon targets. The experiment was done with the EOS Time Project Cahmber (TPC) and multiple sampling ionization chamber (MUSIC II). The TPC provided almost 4π solid angle coverage in the center-of-mass system. Three dimensional tracking and charged particle identification permitted momentum and energy reconstruction of fragments of $1 \leq Z \leq 8$. Particle identification was based on specific energy loss along particle tracks. MUSIC II detected and tracked fragments of $Z \geq 8$. The excellent charge resolution of this detector permitted identification of all detected fragments. The fully reconstructed multifragmentation events for which the total charge of the system was taken as $79 \leq Z \leq 83$, $54 \leq Z \leq 60$, $33 \leq Z \leq 39$ for Au, La, and Kr, respectively [33–35].

The remnant refers to the equilibrated nucleus formed after the emission of prompt particles. The charge and mass of the remant were obtained by removing for each event the total charge of the prompt particles. The excitation energy of the remnant E^* was based on an energy balance between the excited remnant and the final stage of the fragments for each event [36]. The thermal excitation energy E^*_{th} of the remnant is obtained as the difference between E^* and E_x [33–35,37].

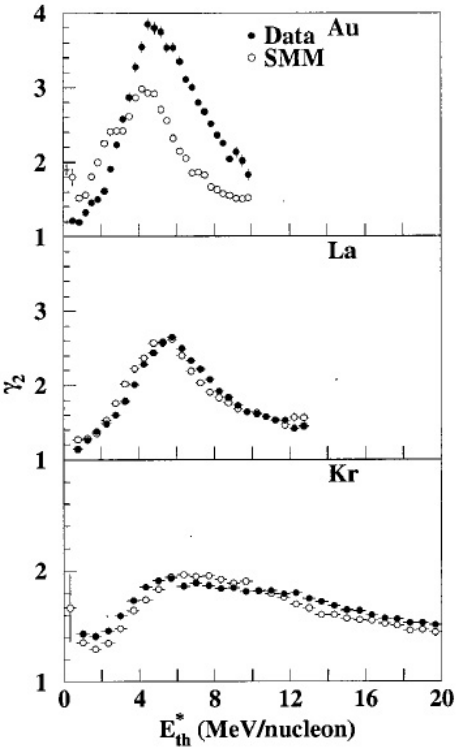

Fig. 4. γ_2 as a function of E^*_{th} for all three systems of 1 A GeV Au, La, and Kr collisions with C target and SMM calculation. Figure is taken from Ref. [33].

4.1.2 Determination of Critical Point and Exponent in Terms of Moment Analysis

γ_2 analysis is shown in Fig. 4 for all three systems. The position of the maximum γ_2 value defines the critical energy E^*_c, which corresponds to the largest fluctuation point in fragment size distribution. The peak in γ_2 is well defined for La and Au. For Kr, the peak is very broad and the value γ_2 is less than 2.

Fig. 4 also shows the γ_2 calculation using SMM where the fission contribution to γ_2 has been removed both from the data and SMM. The peak $\gamma_2 > 2$ for Au and La and $\gamma_2 < 2$ for Kr both from the data and SMM has been observed. In case of Au the γ_2 value remains above two for most of the excitation energy range. The E^*_{th} width over which $\gamma_2 > 2$ is smaller for La and disappears for Kr. The decrease in γ_2 with decrease in system size is also seen in 3D percolation studies and the differences have been attributed to finite size effects [38,39].

In percolation theory, the exponent τ can be obtained if the second moment M_2 and third moment M_3 of the fragment mass distributions are known. A plot of $\ln(M_3)$ vs $\ln(M_2)$ should give a straight line with a slope given by

$$S = \frac{\Delta ln(M_3)}{\Delta ln(M_2)} = \frac{\tau - 4}{\tau - 3}. \quad (9)$$

Fig. 5 shows a scatter plot of $\ln(M_3)$ vs $\ln(M_2)$ for all the three systems from data above E^*_c and from SMM calculation. A linear fit to $\ln(M_3)$ vs $\ln(M_2)$ gives the value τ. The fitted τ values are 2.16 ± 0.08, 2.10 ± 0.06 and 1.88 ± 0.08, respectively. The former two are very close to the critical exponents $\tau \sim 2.3$ of liquid gas universal class. In Fisher model, the thermal critical point is also a critical point for moments of the fragment size distribution. However, this is always true. eg. in the super-critical region of the lattice-gas and realistic Lennard-Jones fluids [80].

The exponent β can be obtained for the multifragmentation data by the relation

$$A_{max} \sim |\epsilon|^{\beta}, \quad (10)$$

where $\epsilon = p - p_c$ and $\epsilon > 0$. In the multifragmentation case p and p_c have been replaced by E^*_{th} and E^*_C. In the infinite system, the finite cluster exists only on the liquid side of p_c. In a finite system a largest cluster is present on both sides of the critical point, but the above equation holds only on the liquid side. Fig. 7 shows a plot of $\ln(A_{max})$ vs $\ln|E^*_{th} - E^*_C|$ from Au, La, and Kr. The values of β extracted for Au and La are 0.32 ± 0.02 and 0.34 ± 0.02, respectively, which is close to the value of 0.33 predicted by a liquid gas phase transition. While the value of $\beta = 0.53 \pm 0.05$ for Kr is much higher than that of Au and La.

As shown in Sec. 2, Campi also suggested that the correlation between the size of the biggest fragment A_{max} and the moments in each event, i.e. the scatter plot, can measure the critical behavior in nuclei. Fig. 7 depicts a scatter plot with logarithmic scale for Au, La, and Kr of EOS data. The two branches corresponding to the sub-critical

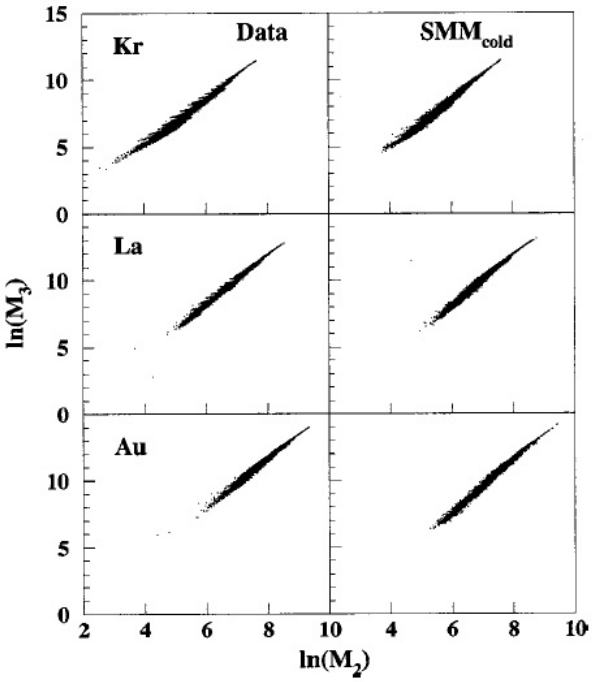

Fig. 5. $\ln(M_3)$ vs $\ln(M_2)$ for Au, La, and Kr above the critical energy. Figure is taken from Ref. [33].

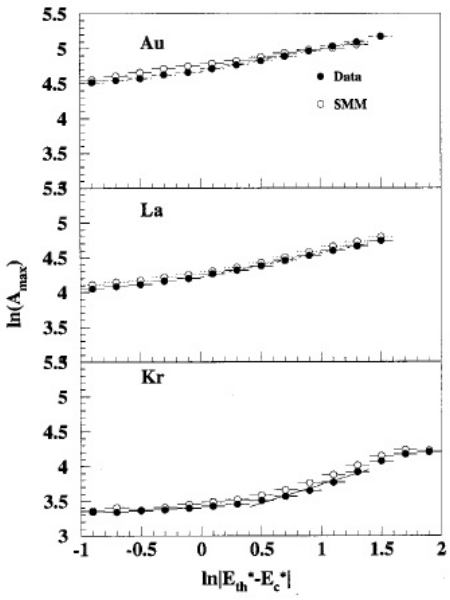

Fig. 6. $\ln(A_{max})$ vs $\ln|E^*_{th} - E^*_C|$ for Au, La, and Kr below the critical energy for exponent β determination. Figure is taken from Ref. [33].

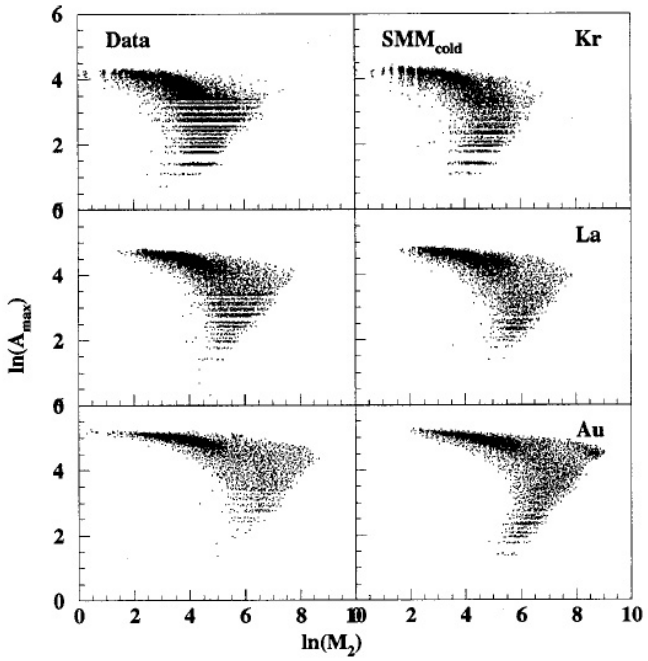

Fig. 7. Scatter plots of $\ln(A_{max})$ vs $\ln(M_2)$ from the data for Au, La, and Kr; (b) Average $\ln(M_3)$ for Au, La, and Kr as a function of $\ln(M_2)$. Figure is taken from Ref. [33].

(upper branch) and overcritical (lower branch) events are clearly seen for Au and La. The scatter plot is very broad for Kr and fills most of the available phase space. The sub- and over-critical branches seem to overlap and are not well separated. Studies on statistical multifragmentation model (SMM) show the similar behavior. If one knows the critical point from some other method, then the scatter plot can be used to calculate the ratio of critical exponents β/γ from the slope of the sub-critical branch. In EOS data, the position of the largest γ_2 was used to define the critical point, which corresponds to the largest fluctuation of the fragment distribution. In this context, β/γ values for Au, La and Kr can be extracted from the linear fit to the upper branch, they are 0.22 ± 0.03, 0.25 ± 0.01 and 0.50 ± 0.01, respectively. β/γ values of Au and La are close to 0.26 of the liquid gas universal class.

4.2 NIMROD data

4.2.1 Experimental set-up and Analysis Details

Using the TAMU NIMROD (Neutron Ion Multidetector for Reaction Oriented Dynamics) and beams from the TAMU K500 super-conducting cyclotron, we have probed the properties of excited projectile-like fragments produced in the reactions of 47 MeV/nucleon ^{40}Ar + ^{27}Al, ^{48}Ti and ^{58}Ni. Earlier work on the reaction mechanisms of near

symmetric collisions of nuclei in the $20 < A < 64$ mass region at energies near the Fermi energy have demonstrated the essential binary nature of such collisions, even at relatively small impact parameters [40]. As a result, they prove to be very useful in preparing highly excited light nuclei with kinematic properties which greatly simplify the detection and identification of the products of their subsequent de-excitation [41].

The charged particle detector array of NIMROD, which is set inside a neutron ball, includes 166 individual CsI detectors arranged in 12 rings in polar angles from $\sim 3^\circ$ to $\sim 170^\circ$. Eight forward rings have the same geometrical design as the INDRA detector, but have less granularity. In these experiments each forward ring included two super-telescopes (composed of two Si-Si-CsI detectors) and three Si-CsI telescopes to identify intermediate mass fragments. The CsI detectors are Tl doped crystals read by photomultiplier tubes. A pulse shape discrimination method using different responses of fast and slow components of the light output of the CsI crystals is employed to identify particles. In the CsI detectors Hydrogen and Helium isotopes were clearly identified and Li fragments are also isolated from the heavier fragments. In the super-telescopes, all isotopes with atomic number $Z \leq 8$ were clearly identified and in all telescopes particles were identified in atomic number. The NIMROD neutron ball, which surrounds the charged particle array, was used to determine the neutron multiplicities for selected events. The neutron ball consists of two hemispherical end caps and a central cylindrical section. The hemispheres are upstream and downstream of the charged particle array. They are 150 cm in diameter with beam pipe holes in the center. The central cylindrical sections 1.25m long with an inner hole of 60 cm diameter and 150 cm outer diameter. It is divided into four segments in the azimuthal angle direction. Between the hemispheres and the central section, there are 20 cm air gaps for cables and a duct for a pumping station. The neutron ball is filled with a pseudocumene based liquid scintillator mixed with 0.3 weight percent of Gd salt (Gd 2-ethyl hexanoate). Scintillation from a thermal neutron captured by Gd is detected by five 5-in phototubes in each hemisphere and three phototubes in each segment of the central section.

The correlation of the charged particle multiplicity (M_{cp}) and the neutron multiplicity (M_n) was used to sort event violence. Recently we have developed a new method for the assignment of each light charged particle (LCP) to an emission source [14]. This is done with a combination of three source fits and Monte-Carlo sampling techniques. We first obtain the laboratory energy spectra for different LCP at different laboratory angles and reproduce them using the three source fits. In the laboratory frame, the energy spectra of LCP can be modelled as the overlap of emission from three independent moving equilibrated sources, *i.e.* the QP, NN and QT sources. Intermediate mass fragments, IMF, with Z≥4 were identified in the telescope modules of NIMROD. For such ejectiles we have we have not used such fitting techniques. Rather we have used a rapidity cut (> 0.65 beam rapidity) to assign IMF to the

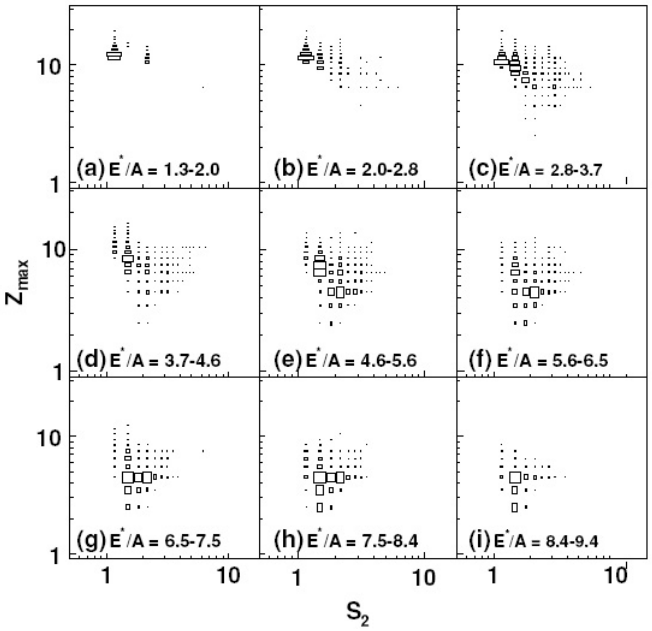

Fig. 8. The Campi plot for different excitation energy windows for the QP formed in ^{40}Ar + ^{58}Ni. Figure is taken from Ref. [14].

QP source. To select the nearly complete QP events, we choose events with $Z_{QP} \geq 12$ (*i.e.* as good events. After the reconstruction of the QP particle source, the excitation energy was deduced event-by-event using the energy balance equation [36].

4.2.2 Critical Point Determination in Terms of Moment Analysis

In Fig. 8 we present such plots for the nine selected excitation energy bins. In the low excitation energy bins of $E^*/A \leq 3.7$ MeV/u, the upper (liquid phase) branch is strongly dominant while at $E^*/A \geq 7.5$ MeV/u, the lower Z_{max} (gas phase) branch is strongly dominant. In the region of intermediate E^*/A of 4.6- 6.5 MeV/u, the transition from the liquid dominated branch to the vapor branch occurs, indicating that the region of maximal fluctuations is to be found in that range.

The excitation energy dependence of the average values of γ_2 obtained in an event-by-event analysis of our data are shown in Fig. 9. γ_2 reaches its maximum in the 5-6 MeV excitation energy range. In contrast to observations for heavier systems of Au and La [33,43], there is no well defined peak in γ_2 for our very light system and γ_2 is relatively constant at higher excitation energies. This is similar to the case of Kr of EOS data. We note also that the peak γ_2 value is lower than 2 which is the expected smallest value for critical behavior in large systems. However, 3D percolation studies indicate that finite size effects

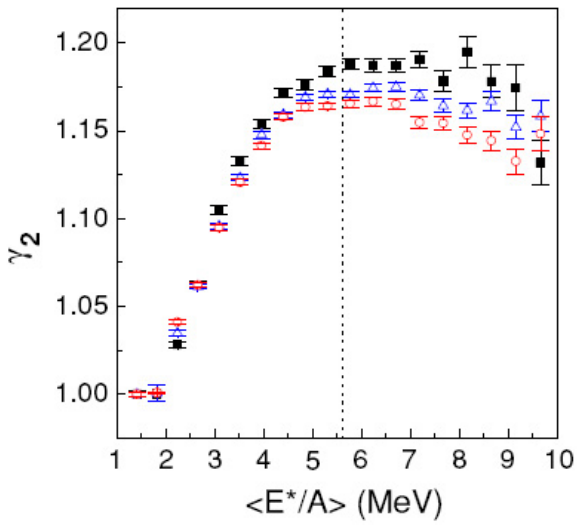

Fig. 9. γ_2 of the QP systems formed in Ar + Al (open circles), Ti (open triangles) and Ni (solid squares) as a function of excitation energy. Figure is taken from Ref. [14].

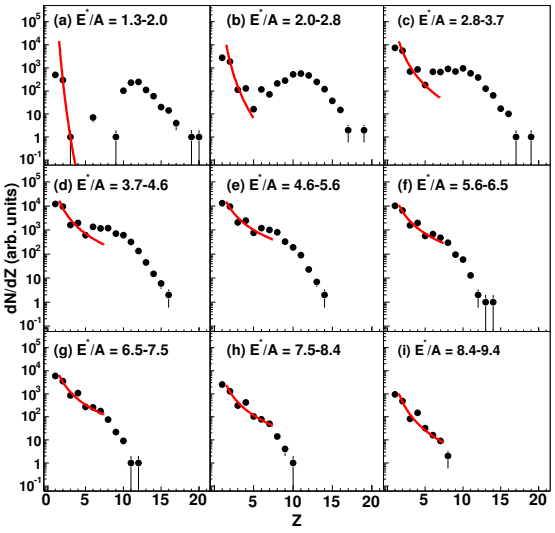

Fig. 10. Charge distribution of QP in different E^*/A window for the reaction ^{40}Ar + ^{58}Ni. Lines represent fits. Figure is taken from Ref. [14].

can lead to a decrease of γ_2 with system size [38,39]. For a percolation system with 64 sites, peaks in γ_2 under two are observed. Therefore, the lone criterion $\gamma_2 > 2$ is not sufficient to discriminate whether or not the critical point is reached.

In the Fisher droplet model, the critical exponent τ can be deduced from the cluster distribution near the phase transition point. To quantitatively pin down the possible phase transition point, we use a power law fit to the QP charge distribution in the range of Z = 2 - 7 to extract the effective Fisher-law parameter τ_{eff} by

$$dN/dZ \sim Z^{-\tau_{eff}}. \quad (11)$$

The Fisher droplet model has been extensively applied to the analysis of multifragmentation. It predicts that relative yields of fragments with $3 \leq Z \leq 14$ could be well described by a power law dependence $A^{-\tau}$ when the liquid gas phase transition occurs and τ value is the minimum in that point. To quantitatively pin down the possible phase transition point, we use a power law fit to the QP charge distribution in the range of Z = 2 - 7 to extract the effective Fisher-law parameter τ_{eff} by $dN/dZ \sim Z^{-\tau_{eff}}$. Fig. 11(a) shows τ_{eff} vs excitation energy, a minimum with $\tau_{eff} \sim 2.3$ is seen to occur in the E^*/A range of 5 to 6 MeV/u. $\tau_{eff} \sim 2.3$, is close to the critical exponent of the liquid gas phase transition universality class as predicted by Fisher's Droplet model [2]. The observed minimum is rather broad.

While, assuming that the heaviest cluster in each event represents the liquid phase, we have attempted to isolate the gas phase by event-by-event removal of the heaviest cluster from the charge distributions. We find that the resultant distributions are better described as exponential

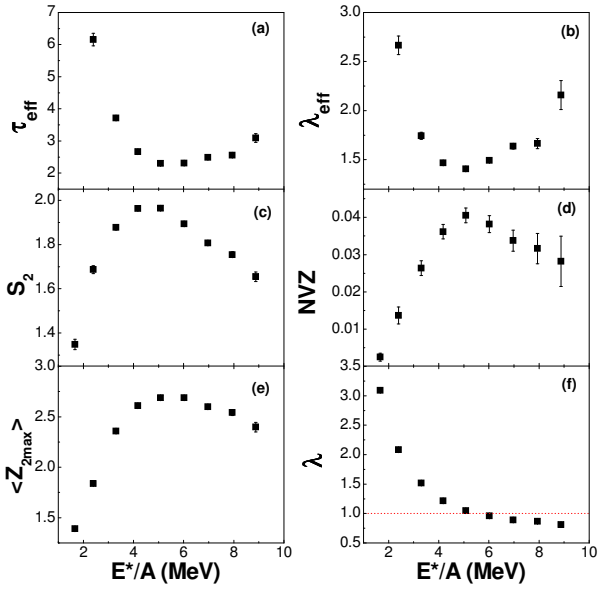

Fig. 11. The effective Fisher-law parameter (τ_{eff}) (a), the effective exponential law parameter (λ_{eff}) (b), $\langle S_2 \rangle$ (c), NVZ fluctuation (d), the mean charge number of the second largest fragment $\langle Z_{2max} \rangle$ (e), the Zipf-law parameter λ (f). See details in text. Figure is taken from Ref. [44].

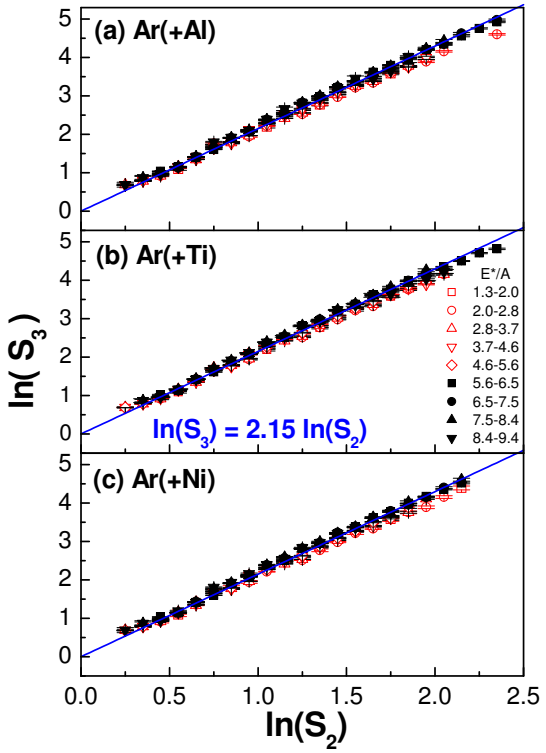

Fig. 12. (Color online) The correlation between $\ln(S_3)$ vs $\ln(S_2)$ and the linear fit. Figure is taken from Ref. [14].

form $exp(-\lambda_{eff}Z)$. The fitting parameter λ_{eff} was derived and is plotted against excitation energy in Fig. 11(b). A minimum is seen in the same region where τ_{eff} shows a minimum. To further explore this region we have investigated other proposed observables commonly related to fluctuations and critical behavior. Fig. 11(c) shows the mean normalized second moment [42], $\langle S_2 \rangle$ as a function of excitation energy. A peak is seen around 5.6 MeV/u, it indicates that the fluctuation of the fragment distribution is the largest in this excitation energy region. Similarly, the normalized variance in Z_{max}/Z_{QP} distribution (i.e. NVZ = $\frac{\sigma^2_{Z_{max}/Z_{QP}}}{\langle Z_{max}/Z_{QP} \rangle}$) [45] shows a maximum in the same excitation energy region [Fig. 11(d)], which illustrates the maximal fluctuation for the largest fragment (order parameter) is reached around $E^*/A = 5.6$ MeV. Except the largest fragment, the second largest fragment also shows its importance in the above turning point. Fig. 11(e) shows a broad peak of $\langle Z_{2max} \rangle$ - the average atomic number of the second largest fragment exists at 5.6 MeV/u.

4.2.3 Critical Exponent Determination Based on Moment Analysis

In terms of the scaling theory, τ can also be deduced from the Eq.(9), shown in Fig. 12. Assuming the value of T_c = 8.3 MeV as determined from our caloric curve measurements [14], we explored the correlation of S_2 and S_3 in two ranges of excitation energy C see Figure. 12. The moments were computed by exclusion of the species with Z_{max} in the "liquid" phase but inclusion in the "vapor" phase.The slopes were determined from linear fits to the "vapor" and "liquid" regions respectively and then averaged. In this way, we obtained a value of $\tau = 2.13 \pm 0.1$. See Fig. 12.

Other critical exponents can also be related to other moments of cluster distribution, M_k, which were defined in Eq.(1). Since, for our system, we have already deduced the initial temperatures and determined a critical temperature $T_c = 8.3$ MeV at point of maximal fluctuations [14], we can use temperature as a control parameter for such determinations. In this context, the critical exponent β can be extracted from the relation

$$Z_{max} \propto (1 - \frac{T}{T_c})^{\beta}, \tag{12}$$

and the critical exponent γ can be extracted from the second moment via

$$M_2 \propto |1 - \frac{T}{T_c}|^{-\gamma}. \tag{13}$$

In each, $|1 - \frac{T}{T_c}|$ is the parameter which measures the distance from the critical point.

Fig. 13 explores the dependence of Z_{max} on $(\frac{T}{T_c})$. We note a dramatic change of Z_{max} around the critical temperature T_c. LGM calculations also predict that the slope of Z_{max} vs T will change at the liquid gas phase transition [46]. Physically, the largest fragment is simply related to the order parameter $\rho_l - \rho_g$ (the difference of density in nuclear 'liquid' and 'gas' phases). In infinite matter, the infinite cluster exists only on the 'liquid' side of the critical point. In finite matter, the largest cluster is present on both sides of the phase transition point. In this figure, the significant change of the slope of Z_{max} with temperature should correspond to a sudden disappearance of the infinite cluster ('bulk liquid') near the phase transition temperature. For the finite system, it reflects the onset of critical behavior there. Using the left side of this curve (*i.e.* liquid side), we can deduce the critical exponent β by the transformation of the x axis variable to the distance from the critical point. Fig. 13b shows the extraction of β using Eq. 12. An excellent fit was obtained in the region away from the critical point, which indicates a critical exponent $\beta = 0.33 \pm 0.01$. Near the critical point, the finite size effects become stronger so that the scaling law is violated. The extracted value of β is that expected for a liquid gas transition (See Table.II) [30].

To extract the critical exponent γ, we take M_2 on the liquid side without Z_{max} but take M_2 on the vapor side with Z_{max} included. Fig. 14 shows $\ln(M_2)$ as a function of $\ln(|1-\frac{T}{T_c}|)$. The lower set of points is from the liquid phase and the upper set of points is from the vapor phase. For the liquid component, we center our fit to Eq. 13 about the center of the range of $(1 - T/T_c)$ which leads to the linear fit and extraction of β as represented in Figure. 13. We obtain the critical exponent $\gamma = 1.15 \pm 0.06$. This value of γ is also close to the value expected for the liquid

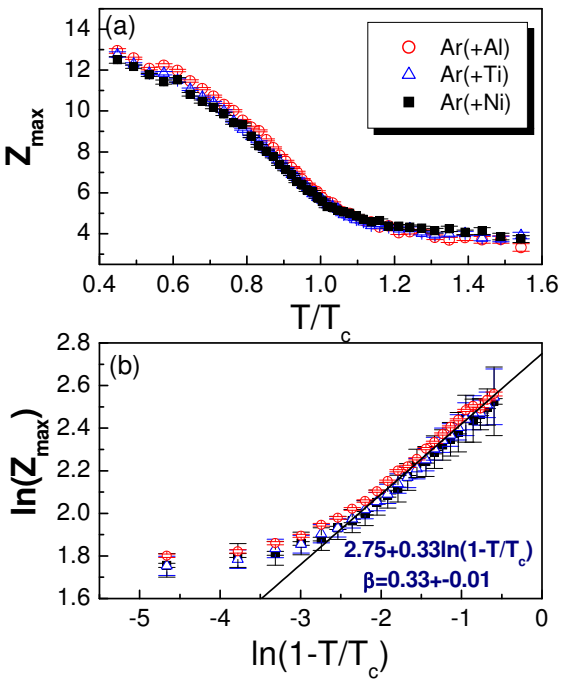

Fig. 13. (Color online) Z_{max} as a function of T/T_c (a) and the extraction of the critical exponent β (b). Figure is taken from Ref. [14].

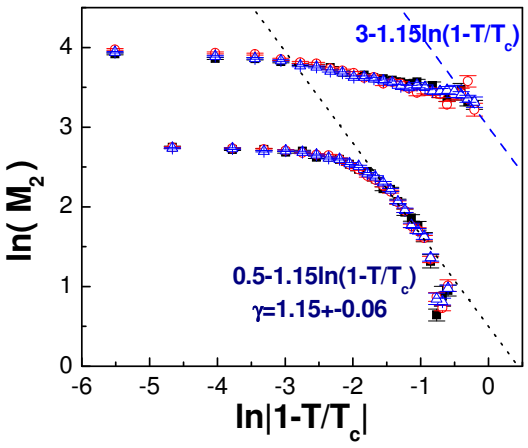

Fig. 14. The extraction of critical exponents γ. See texts for details. Figure is taken from Ref. [14].

Table 1. Comparison of the Critical Exponents

Exponents	3D Percolation	Liquid-Gas	NIMROD Data
τ	2.18	2.21	2.13±0.10
β	0.41	0.33	0.33±0.01
γ	1.8	1.23	1.15±0.06
σ	0.45	0.64	0.68±0.04

gas universality class (see Table II). It is seen that the selected region has a good power law dependence. However, a similar effort to extract the γ in the gas phase is not successful: a small value less than 0.20 is deduced. This may be due to the finite size effects for this very light system. Since the largest cluster still exists in the vapor side, its inclusion (or exclusion) in M_2 might perturb the determination of the moment, resulting in an imprecise value of γ extracted from the vapor phase. For comparison, we just show, for the vapor phase, a line representing the γ derived from the liquid side. This line only agrees with the last few vapor points, *i.e.* the highest temperature points (the contamination of M_2 should the least there).

Since we have the critical exponent β and γ, we can use the scaling relation

$$\sigma = \frac{1}{\beta + \gamma}, \tag{14}$$

to derive the critical exponent σ. In such way, we get the $\sigma = 0.68 \pm 0.04$, which is also very close to the expected critical exponent of a liquid gas system.

Finally, it is possible to use the scaling relation

$$\tau = 2 + \frac{\beta}{\beta + \gamma}, \tag{15}$$

to check the τ value which was determined from the charge distributions using Fisher droplet model power law fits around the critical point (see Fig. 10). Using Eq. 15 we Obtain $\tau = 2.22 \pm 0.46$, which, though less precise, is in agreement with the values of 2.31 ± 0.03 obtained from the charge distribution around the point of maximal fluctuations and 2.15 ± 0.1 extracted from the correlation of $\ln(S_3)$ vs $\ln(S_2)$.

To summarize critical exponents of the NIMROD data, we present the results in Table.II as well as the values expected for the 3D percolation and liquid gas system universality classes. Obviously, our values for this light system with A$\sim$36 are consistent with the values of the liquid gas phase transition universality class rather the 3D percolation class.

5 Scaled factorial moments and intermittency

Except the moment of fragment size distribution, there is another moment, namely scaled factorial moment which is common used in the study of the intermittency [47]. It was introduced into the study of nuclear fragmentation at intermediate energy heavy ion collisions some year ago [48] and it is related to event-by-event fluctuation. One of the motivation for intermittency studies was the ideal of self-similarity on small scales, an ideal borrowed from chaos theories. It was proposed that an intermittency pattern of fluctuations in the fragmentation charge distributions could be observed both in data and in models. Much efforts have been devoted to find the relation between this

fragmentation, a possible liquid gas phase transition and intermittency [42,52,45,49–52].

Generally, intermittency is related to the existence of large nonstatistical fluctuation and is a signal of self-similarity of the fluctuation of the distribution at all scales. This signal can be deduced from the scaled factorial moments [47],

$$F_k(\delta) = \frac{\Sigma_{i=1}^{X_{max}/\delta}\langle n_i(n_i-1)(n_i-2)...(n_i-k+1)\rangle}{\Sigma_{i=1}^{X_{max}/\delta}\langle n_i\rangle^k} \tag{16}$$

where X_{max} is an upper characteristic value of the system (i.e. total mass or charge, maximum transverse energy or momentum, etc.) and k is the order of the moment. The total interval 0-X_{max} (1-A_{max}, Z_{max} in the case of mass or charge distributions) is divided into X_{max}/δ bins of the size δ, n_i is the number of particles in the ith bin for an event, and the ensemble average $\langle\rangle$ is performed over all events. F_k eliminates statistical noise from Poisson distribution. Intermittency is defined by a relation

$$F_k(\delta') \equiv F_k(a\delta) = a^{-f(k)}F_k(\delta), \tag{17}$$

between factorial moments $F_k(\delta')$ and $F_k(\delta_s)$ obtained for two different binning parameters δ and $\delta' = \mathrm{a}\delta$. Here $f(k)$ is the fractal intermittency exponent which is related to the factorial dimension d_k by $f(k) = d_k(k-1) > 0$. Intermittency implies linear relationship in the double logarithmic plot of lnF_k versus $-ln\delta$.

Several models have been proposed to describe the multfragmentation of nuclear systems and to study the intermittency signal. One of the simplest models, wildly used in the analysis of experimental data and which gives intermittency, is the percolation model. Percolation models predict a phase transition corrected for finite size effects and produce, at the critical point for this phase transition, a mass distribution following a power law and obeying the scaling properties.

In order to relate the intermittency and critical behavior, the anomalous fractal dimension d_i connected to the intermittency exponents λ_i by

$$d_i = \lambda_i/(i-1). \tag{18}$$

Different processes seem to give a different behavior of these anomalous fractal dimension d_i: (1) d_i = constant corresponds to a monofractal, second order phase transition in the Ising model and in the Feyman-Wilson fluid; (2)$d_i \propto i$ correspond to multifractal, cascading processes. Therefore, a study of the anomalous fractal dimensions can give useful information about the evolution of the system.

Intermittency analysis has been attempted in many heavy ion collision data as well as emulsion data. Here we gave an example of the multifragmentation data of Au + Au collisions at 35 MeV/u which was performed at MSCL by the Multics-Miniball Collaboration [53]. A power-law charge distribution, $A^{-\tau}$ with $\tau \simeq 2.2$ and an intermittency signal has been observed for the events selected in the region of Campi scatter plot where "critical" behavior is expected. As shown in Fig. 15, three cuts have been

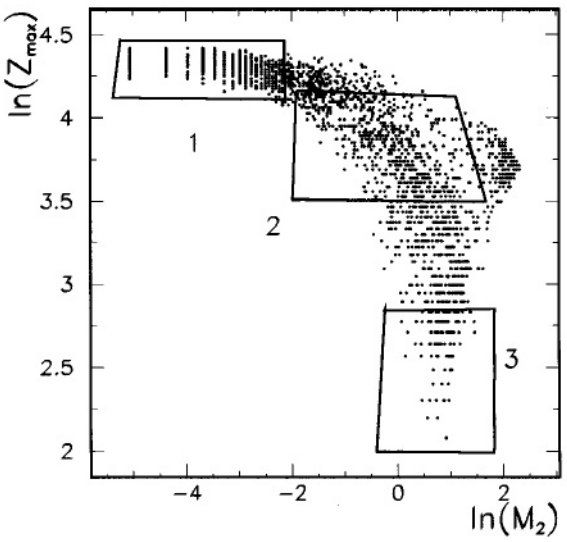

Fig. 15. Experimental results from Ref. [53]. Campi scatter plot. Three cuts are employed to selected the upper branch (1), the lower branch (3), and the central region (2).

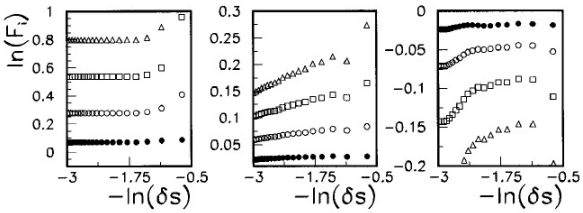

Fig. 16. Experimental results from Ref. [53]. Scaled factorial moments $\ln(F_i)$ vs -$\ln(\delta_s)$ for the three cuts made on Fig. 15: left part cut 1, central part cut 2, and right part cut 3. Solid circles represent the SFM of order i=2, open circles i = 3, open squares i = 4, and open triangles i = 5. Figure is taken from Ref. [53].

tested. The upper branch is mostly related to the liquid branch and the lower branch the gas branch. While the central cut (2) is expected to a region where the critical behavior takes place. Actually the resultant charge distribution of the cut (2) has a power-law distribution with $\tau \simeq 2.2$ which is close to the droplet model prediction if the liquid gas phase transition occurs. For cut 3, the logarithm of the scaled factorial moment is always negative and almost independent on -lnδs; there is no intermittency signal. The situation is different for cut 2 (the central part). The logarithm of scaled factorial moment is positive and almost linearly increasing as a function of -lnδs, and an intermittency has been observed. Cut 1 gives a zero slope, no intermittency signal again. The interpretation of experimentally observed intermittency signal may, however, problematic due to the ensemble average effect [49]. Since cut 2 involves a large range of impact parameters, the observed intermittency signal could be an artifact of ensemble averaging, and can not be seen as a definite evidence of large fluctuation driven by the critical behavior.

Actually, several criticisms have been raised about the role of the intermittency signal in nuclear fragmentation and the nuclear phase transition. For instance, Elatteri et al. showed that an intermittency signal can be obtained even for a simple fragmentation generator model by the random population of mass bins with a power law distribution in which the only nonstatistical source of fluctuations is the mass conservation law [50]. It has also been shown that the intermittency signal is washed out when events of fixed total multiplicity are selected [42,45] or when the size of the system tends to infinity in the percolation model in which the fluctuations are of nontrivial origin [42]. Moreover, the intermittency signal is not observed in the narrow excitation energy region where the phase transition occurs in the framework of the well-known Copenhagen statistical multi-fragmentation model [51] or in the data of 35-110 MeV/nucleon $^{36}Ar + ^{197}Au$ when the effects of impact parameter averaging are reduced by some appropriate cuts [49].

For an example, we check the intermittency behavior [54] in the Lattice Gas model for the disassembly of the system ^{129}Xe at $0.38\rho_0$ in the framework of LGM (for the details of the model description, please see the following section). At temperature $T = 5.5$ MeV, the mass distribution shows a power-law distribution with the effective power-law parameter $\tau = 2.43$. In the previous work with the same model and parameters, it was shown that the liquid gas phase transition occurs near 5.5 MeV for this system [55,68]. The lnF_k shows slight negative values with a slight positive slopes versus $-ln\delta$. However, this kind of the positive slopes with the moment less than unity may be trivial origin and does not illustrate the appearance of the intermittency which is generally sough for systems exhibiting larger than Poisson fluctuations (i.e. the moment should be larger than unity). In order to check the event mixture effect on the scaled factorial moment, we mixed all the events at $T = 4$ MeV and $T = 7$ MeV and also used the multiplicity cuts ($29 \leq M \leq 101$) and ($M < 29$ or $M > 101$) to see if there exits the intermittency behavior in such mixed events. Figure. 17 shows these results. Even though all the lnF_k values are positive, they are flat, i.e. there is no intermittency signal. In these cases, the fluctuation is large enough but the mass distribution shows no power-law distribution. Hence, intermittency is absent. However, intermittency emerges when the moments were calculated from the mixed events of $T = 5.5$ MeV and $T = 7$ MeV (Figure. 17). In this case, the mass distribution shows a quite good power-law distribution and fluctuations are also large enough to induce the intermittency.

From the above discussions, the intermittency seems not a good signal to probe the critical behavior.

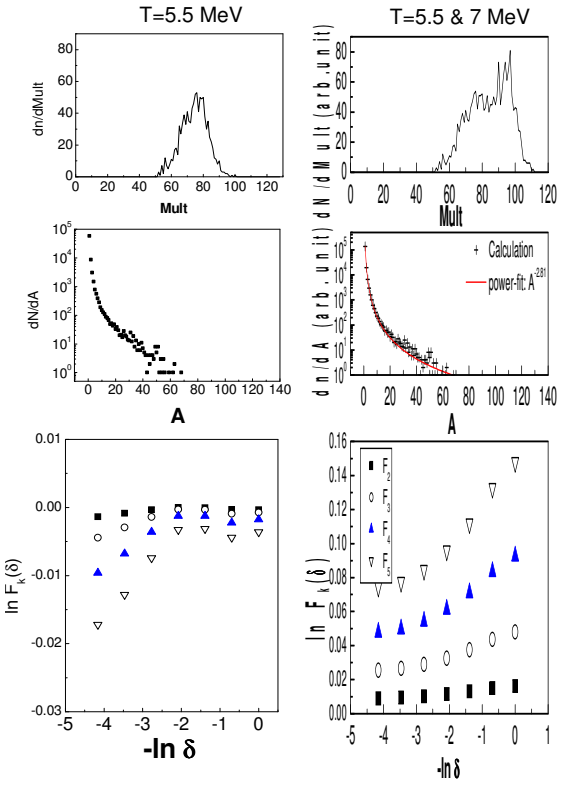

Fig. 17. (Color online) Left panels: the multiplicity distribution (upper panel), the mass distribution (middle panel), the scaled factorial moment (bottom panel); Right panel: Same as the left panel but for the events mixed with $T = 5.5$ MeV and $T = 7$ MeV with the multiplicity restriction for ^{129}Xe in the lattice gas model calculation. Figure is taken from Ref. [54].

6 Phenomenological Base of Nuclear Zipf Law

In above sections, we focus on the moment analysis, namely the moment of the ragment size distribution or the scaled factorial moment. Both are related to the fluctuations of some physical observables. In this section, we would like to emphasize the topological structure of the fragment size distribution, i.e. how the fragments distribute from the largest to the smallest in the nuclear fragmentation. To this end, we introduced the Zipf-type plot, i.e. rank-ordering plot, in fragment size distribution as well as Zipf's law which will be illustrated in the following [55,56].

The original Zipf's law [57] has been introduced into the diagnosis of nuclear liquid gas phase transition and we called it as nuclear Zipf's law. Zipf's law has been known as a statistical phenomenon concerning the relation between English words and their frequency in literature in the field of linguistics [57]. The law states that, when we list the words in the order of decreasing population, the frequency of a word is inversely proportional to its rank [57]. This relation was found not only in linguistics but also in other fields of sciences. For instance, the law appeared in distributions of populations in cities, distributions of income of corporations, distributions of areas of lakes and cluster-size distribution in percolation process [58,59]. The details for the proposal of nuclear Zipf's law can been found in Ref. [55,56]. In this report, we firstly define the nuclear Zipf plot for the fragment mass (charge)

distribution and nuclear Zipf's law in the simulation with help of the lattice gas model. Then we show the evidence of nuclear Zipf law around the liquid gas phase transition. Finally we give conclusion and outlook.

6.1 Model Simulations

The tools we will use here are the isospin dependent lattice gas model (LGM) and molecular dynamical model (MD). The lattice gas model was developed to describe the liquid-gas phase transition for atomic system by Lee and Yang [60]. The same model has already been applied to nuclear physics for isospin symmetrical systems in the grandcanonical ensemble [61] with a sampling of the canonical ensemble [62–68], and also for isospin asymmetrical nuclear matter in the mean field approximation [69]. In addition, a classical molecular dynamical model is used to compare its results with the results of lattice gas model. Here we will make a brief description for the models.

In the lattice gas model, A $(= N + Z)$ nucleons with an occupation number s which is defined $s = 1$ (-1) for a proton (neutron) or $s = 0$ for a vacancy, are placed on the L sites of lattice. Nucleons in the nearest neighboring sites interact with an energy $\epsilon_{s_i s_j}$. The hamiltonian is written as $E = \sum_{i=1}^{A} \frac{P_i^2}{2m} - \sum_{i<j} \epsilon_{s_i s_j} s_i s_j$. The interaction constant $\epsilon_{s_i s_j}$ is chosen to be isospin dependent and be fixed to reproduce the binding energy of the nuclei [66]:

$$\begin{aligned} \epsilon_{nn} &= \epsilon_{pp} = 0.MeV, \\ \epsilon_{pn} &= -5.33MeV. \end{aligned} \tag{19}$$

A three-dimension cubic lattice with L sites is used. The freeze-out density of disassembling system is assumed to be $\rho_f = \frac{A}{L}\rho_0$, where ρ_0 is the normal nuclear density. The disassembly of the system is to be calculated at ρ_f, beyond which nucleons are too far apart to interact. Nucleons are put into lattice by Monte Carlo Metropolis sampling. Once the nucleons have been placed we also ascribe to each of them a momentum by Monte Carlo samplings of Maxwell-Boltzmann distribution.

Once this is done the LGM immediately gives the cluster distribution using the rule that two nucleons are part of the same cluster if $P_r^2/2\mu - \epsilon_{s_i s_j} s_i s_j < 0$. This method is similar to the Coniglio-Klein's prescription [70] in condensed matter physics and was shown to be valid in LGM [62,63,65,67]. To calculate clusters using MD we propagate the particles from the initial configuration for a long time under the influence of the chosen force. The form of the force is chosen to be also isospin dependent in order to compare with the results of LGM. The potential for unlike-nucleons is

$$\begin{aligned} v_{\rm np}(r)(\frac{r}{r_0} < a) &= C\left[B(\frac{r_0}{r})^p - (\frac{r_0}{r})^q\right] e^{-\frac{1}{(\frac{r}{r_0}-a)}}, \\ v_{\rm np}(r)(\frac{r}{r_0} > a) &= 0. \end{aligned} \tag{20}$$

where $r_0 = 1.842fm$ is the distance between the centers of two adjacent cubes. The parameters of the potentials are $p = 2$, $q = 1$, $a = 1.3$, $B = 0.924$, and $C = 1966$ MeV. With these parameters the potential is minimum at r_0 with the value -5.33 MeV, is zero when the nucleons are more than $1.3r_0$ apart and becomes strongly repulsive when r is significantly less than r_0. The potential for like-nucleons is written as

$$\begin{aligned} v_{\rm pp}(r)(r < r_0) &= v_{\rm np}(r) - v_{\rm np}(r_0), \\ v_{\rm pp}(r)(r > r_0) &= 0. \end{aligned} \tag{21}$$

The system evolves with the above potential. At asymptotic times the clusters are easily recognized. Observables based on the cluster distribution in the both models can now be compared. In the case of proton-proton interactions, the Coulomb interaction can also be added separately and it can be compared with the case without Coulomb effects.

In the simulation part of this report we choose the medium size nuclei ^{129}Xe as an example. In most cases, ρ_f is chosen to be 0.38 ρ_0, since the experimental data can be best fitted by ρ_f between $0.3\rho_0$ and $0.4\rho_0$ in previous LGM calculations [65,71], which corresponds to 7^3 cubic lattice.

In order to check the phase transition behavior in the I-LGM, we will firstly show the results of some physical observables, namely the effective power-law parameter, τ, the second moment of the cluster distribution, S_2 [42], and the multiplicity of intermediate mass fragments, N_{imf} for the disassembly of ^{129}Xe in figure 1. These observables have been evidenced useful in previous works to judge the liquid gas phase transition, as shown in Ref. [66,72,68]. The valley of τ, the peaks of N_{imf} and S_2 happens around $T \sim 5.5$ MeV which is the signature of onset of phase transition. The above phase transition temperature will be only used as a reference of the novel signature, as stated below.

Now we present the results for testing Zipf's law in the charge distribution of clusters. The law states that the relation between the sizes and their ranks is described by $Z_n = c/n$ (n=1, 2, 3, ...), where c is a constant and Z_n is the average charge (or mass) of rank n in a charge (or mass) list when we arrange the clusters in the order of decreasing size. For instance the charge Z_2 of the second largest cluster with rank $n = 2$ is one-half of the charge Z_1 of the largest cluster, the charge Z_3 of the third largest cluster with rank $n = 3$ is one-third of the charge Z_1 of the largest cluster, and so on. In the simulations of this work, we averaged the charges for each rank in charge lists of the events: we averaged the charges for the largest clusters in each event, averaged them for the second largest clusters, averaged them for the third largest clusters, and so on. From the charges averaged, we examined the relation between the charges Z_n and their ranks n. Figure 2 shows such relations of Z_n and n for Xe in different temperature. The histogram is the simulated results and the straight lines represent the fit with $Z_n \propto n^{-\lambda}$ in the range of $1 \leq n \leq 10$, where λ is the slope parameter. λ is 5.77 at $T = 3$ MeV. Then we increased the temperature and examined the same relation and obtained $\lambda = 3.65$ and 1.53 at $T = 4$ and 5 MeV, respectively. Up to $T = 5.5$ MeV, λ

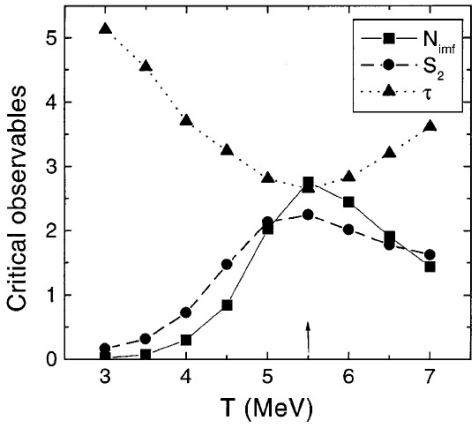

Fig. 18. The effective power-law parameter, τ, the second moment of the cluster distribution, S_2, and the multiplicity of intermediate mass fragments, N_{imf} as a function of temperature for the disassembly of ^{129}Xe. The arrow represents the position of phase transition temperature. Figure is taken from [56].

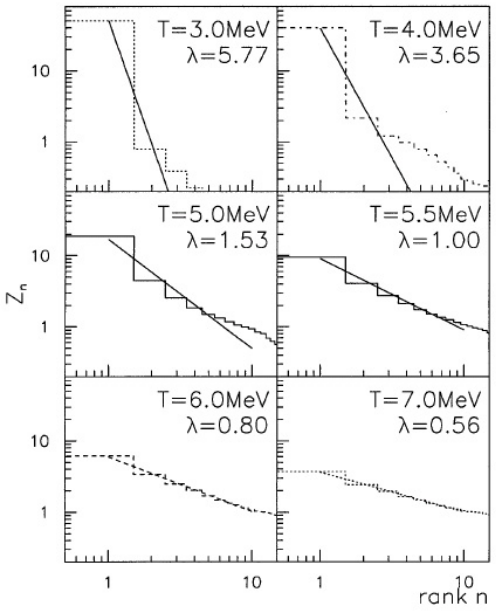

Fig. 19. The average charge Z_n with rank n as a function of n for ^{129}Xe. The histograms are the calculation results and the straight lines are their fits with $Z_n \propto n^{-\lambda}$. Figure is taken from [56].

= 1.00, i.e., at this temperature the relation is satisfied to the Zipf's law: $Z_n \propto n^{-1}$. When temperature continues to increases, λ continues to decreases, for instance, $\lambda = 0.80$ at $T = 6$ MeV and $\lambda = 0.56$ at $T = 7$. This temperature having the Zipf's law, denoted as T_A, is consistent with the phase transition temperature obtained in Fig. 1, illustrating that the Zipf's law is also a good judgement to phase transition. From the statistical point of view, the Zipf's law is related to the critical phenomenon [2,30]. Figure 3a summarizes the parameter λ as a function of temperature. Clearly the Zipf's law ($\lambda = 1$) reveals at phase transition point.

In order to further illustrate that the Zipf's law exists most probably in phase transition point, we directly reproduce the histograms with Zipf's law: $Z_n = c/n$. In this case, c is sole parameter, but what we are interesting in is its truth of the hypothesis of Zipf's law: the χ^2 test. Figure 3b demonstrates the χ^2/ndf for the Z_n - n relations at different T. As expected, there is the minimum χ^2/ndf around the phase transition temperature, which further support that Zipf's law of the fragment distribution reveals when the liquid gas phase transition occurs.

Beside $0.38\rho_0$ was used for ^{129}Xe, $0.18\rho_0$, corresponding to 9^3 cubic lattice and $0.60\rho_0$, corresponding to 6^3 cubic lattice of ρ_f are also taken to compare and check the results with different ρ_f values in the LGM case. It was found that the Zipf's law is also valid when the liquid gas phase transition occurs at different freeze-out density. Moreover, we also investigated larger systems, such as A = 274, 500 and 830, in the LGM case to see if the system behaves as expected in ^{129}Xe. The results show that the Zipf's law behavior still remains at the same phase transition temperature as the one extracted from the extreme values of τ, N_{imf} and S_2. It illustrates that nuclear Zipf's law is suitable as a signal of phase transition in larger A limit.

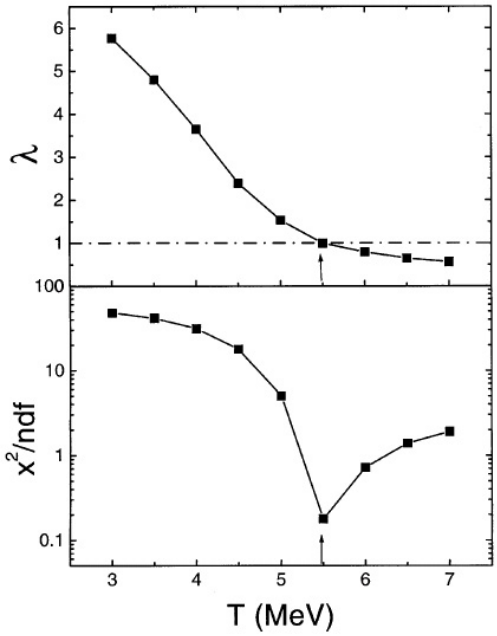

Fig. 20. The slope parameter λ of Z_n to n (a) and the χ^2 test for Zipf's law (b) as a function of temperature for ^{129}Xe. The arrow represents the position of phase transition temperature. Figure is taken from [56].

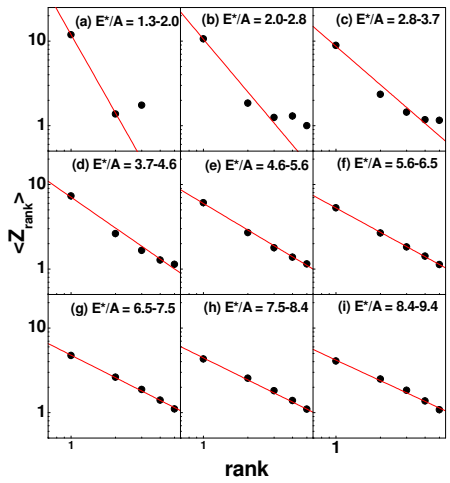

Fig. 21. Zipf plots in nine different excitation energy bins for the QP formed in ^{40}Ar + ^{58}Ni. The dots are data and the lines are Zipf-law fits. The statistical error is smaller than the size of the circles. Figure is taken from [14].

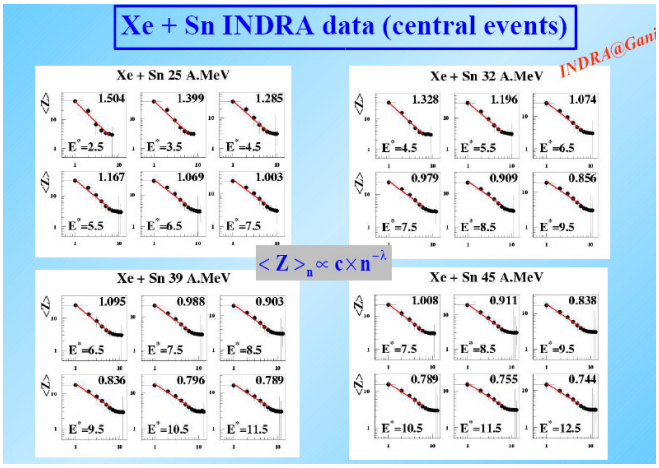

Fig. 22. Nuclear Zipf-type plots for the Xe + Sn systems at 25 MeV/u, 32 MeV/u, 39 MeV/u and 45 MeV/u. Fuigure is atken from IWM05 talk of Le Neindre. Figure is taken from [73].

7 Experimental evidences of Nuclear Zipf Law

7.1 NIMROD results

In Sec. 3.2, we give some information on critical exponent analysis based on moment analysis technique for the Texas A&M NIRMOD data. Some coherent information on critical behavior has been shown. In this section, we will show the further significance of the 5-6 MeV region in NIMROD data by a Zipf's law analysis. In Fig. 21 we present Zipf plots for rank ordered average Z in the nine different energy bins. Lines in the figure are fits to the power law expression $\langle Z_n \rangle \propto n^{-\lambda}$. Fig. 11(f) shows the fitted λ parameter as a function of excitation energy. As shown in Fig. 21, this rank ordering of the probability observation of fragments of a given atomic number, from largest to the smallest, does indeed lead to a Zipf's power law parameter $\lambda = 1$ in the 5-6 MeV/nucleon range. When $\lambda \sim 1$, Zipf's law is satisfied. In this case, the mean size of the second largest fragment is 1/2 of that of the the largest fragment; That of the third largest fragment is 1/3 of the largest fragment, etc.

7.2 INDRA@GANIL Experiment

Zipf's law in nuclear multifragmentation experiment by INDRA at GANIL has been also checked recently [73]. A good coherence between different signals of the critical behaviors and the Zipf's law has been obtained for the central collisions Xe + Sn and Ni + Ni. Fig. 22 shows the nuclear Zipf's plots for Xe + Sn systems at different beam energies, namely 25 MeV/u, 32 MeV/u, 39 MeV/u and 45 MeV/u, respectively. In each panel, six excitation energy windows are plotted. From these plots, the Zipf's law is approximately satisfied around the 7.5 MeV/u of excitation energy where the other observables also indicate the critical behavior regardless of the beam energies. The similar observation has been reached for the system of Ni + Ni [73].

7.3 CERN Emulsion Experiment

The nuclear Zipf-type plot has been also applied in the analysis of CERN emulsion or Plastic data of Pb + Pb or Plastic at 158 AGeV and it was found that the nuclear Zipf law is satisfied when the liquid gas phase transition occurs [74, 75].

Dabrowska et al. extends the studies to the multifragmentation of lead projectiles at an energy of 158 AGeV [74]. The analyzed data were obtained from the CERN EMU13 experiment in which emulsion chambers, composed of nuclear target foils and thin emulsion plates interleaved with spacers, allow for precise measurements of emission angles and charges of all projectile fragments emitted from Pb-Nucleus interactions. The results on fragment multiplicities, charge distributions and angular correlations are analyzed for multifragmentation of the Pb projectile after an interaction with heavy (Pb) and light (Plastic - $C_5H_4O_2$) targets. Detailed description of the emulsion experiment can be found that in Ref. [74].

Fig. 23 shows the Zipf-type plot for the charged fragments heavier than helium emitted in multifragmentation process of Au or Pb projectile at different primary energies. The values of λ exponents from fits $\langle Z_n \rangle \sim n^{-\lambda}$ are

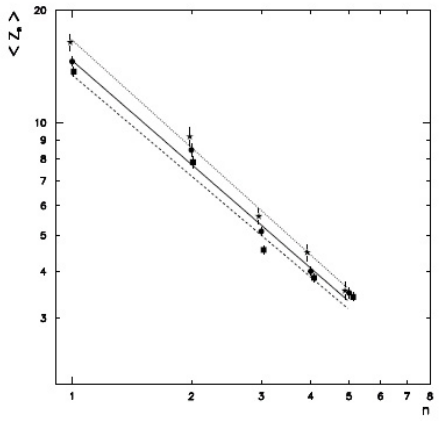

Fig. 23. Zipf law fit to the dependences of the mean charge of the fragment on its rank. The different symbols represent the multfragmentation data of different beam with emulsion target. Circles and solid line represent Pb beam at 158 AGeV, squares and dashed line represents Au beam at 10.6 AGeV, star and dotted line represent Au beam at 0.64 AGeV. The data is taken from Ref. [74].

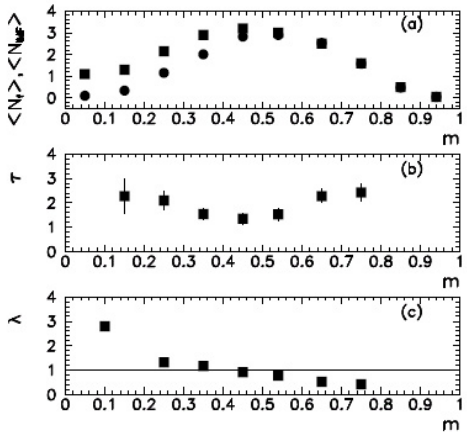

Fig. 24. (a) Mean number, $\langle N_f \rangle$, of fragments (squares) and mean number, $\langle N_{IMF} \rangle$, of intermediate mass fragments (circles) as a function of the normalized multiplicity m. Error bars are smaller than the size of the squares and circles. (b) Power law exponent, τ, of the charge distribution of fragments in different intervals of m. (c) Power law exponent, λ, in the Zipf's law (see text) in different intervals of m. Error bars are smaller then data points. The data is taken from Ref. [75].

0.92 ± 0.03, 0.90 ± 0.02 and 0.96 ± 0.04 for primary energies of 158, 10.6 and 0.64 AGeV, respectively. Within the statistical errors the values of the λ coefficient are the same in the studied energy interval ($<$ 1-158) AGeV and do not differ significantly from unity [74].

Dabrowska et al. also studied the dependence of the power law exponent λ on the control parameter m, the normalized multiplicities by the total charge of spectator particles [75]. In Fig. 24(a) the mean multiplicity $\langle N_f \rangle$ of fragments with $Z \geq 3$ and the mean number $\langle N_{IMF} \rangle$ of the intermediate fragments. The latter are usually defined as fragments with $3 \leq Z \leq 30$. In Fig. 24(b) the dependence of the exponent τ of the power fits to the charge distribution of fragments, perfomed at different ranges of m. In this analysis the fits are restricted to fragment charges smaller than $Z = 16$. At small values of m a system has few light fragments and the power law is steep; at large values of m there are many light fragments and little else leading again a steep power law. At the moderate excitation energies where heavier fragments appear and where we expect the phase transition, the exponent τ has its lowest value. As can be seen from Fig. 24(b) it happens for m values between 0.35 and 0.55. In Fig. 24(c) the dependence of λ obtained from the fits $\langle Z_n \rangle \sim n^{-\lambda}$, on m is depicted. The exponent λ decreases with increasing m from about 0.3 to 0.5 the value of λ is close to unity and the Zipf's law is satisfied. This suggest that at this value of m the liquid gas phase transition occurs. It has been checked that $\lambda = 1$ occurs in the same region of m irrespectively of the mass of the target [75]. This means that the liquid gas phase transition occurs when a given amount of energy is deposited into the nucleus and does not depend on the mass of the target. As expected for liquid gas phase transition, the previously shown maxima in frequency distributions of multiply charged fragments (Fig. 24(a)) as well as a minimum of the power law parameter τ (Fig. 24(b)), all occur at the same values of m, where Zipf's law is satisfied.

7.4 Some remarks on Zipf Law

Recently some remarks were raised on the nuclear Zipf law proposed by the present author. Campi et al. pointed that for the infinite system, Zipf's law is mathematical consequence of a power law cluster size distribution with exponent $\tau \simeq 2$ [76]. More precisely, both Zipf exponent λ and τ are connected through the formula $\lambda = 1/(\tau - 1)$ *for the infinite system* and assuming that the cluster size distribution is power-law distribution in their paper (they ignored a significant early paper of deducing this relationship [78]). They argue that such distributions appear at the critical point with $\tau \simeq 2$ of many theories, eg. various theories of cluster formation (Fischer droplets [2], lattice-gas [60], Lennard-Jones fluids with Hill's clusters [79], percolation [30]) etc., but also elsewhere, eg. in the super-critical region of the lattice-gas and realistic Lennard-Jones fluids [80]. However, the experimental fragmental size distribution is mostly neither power law distribution nor exponential distribution except for some special situation. Also, the nuclear system is always a finite system, which means that the relationship of λ and τ is not strictly valid. Hence, Campi's arguements are not bread-and-butter in the practical viewpoint. Bauer et al. [77] suggested to extend the simple Zipf's law to a more general Zipf-Mandelbrot distribution [81,82], $\langle A_r \rangle = c(r + k)^{-\lambda}$, where the offset k is an additional constant that one has to introduce, and λ is asymptotically approximated as a function of the critical exponent τ, $\lambda(\tau) = 1/(\tau - 1)$ for infinite system. However, the physical meaning of the parameter k is not clear and direct. One can always attempt to extend the simple

formula to the complicate forms by introducing more free parameters, but the cost is weakening physical meaning of the original formula. Overall, we think that Zipf-type plot is a kind of direct observable to characterize the fragment hierarchy in nuclear disassembly and is useful to serve as a signal of phase transition as some data already show in above.

8 Summary

In summary, moment analysis method has been introduced and some applications to the nuclear multifragmentation have been presented. The critical behavior of nuclear disassembly can be investigated with help of moment analysis and some critical exponents could be determined. In addition, finite size effect is also discussed in the model calculation. Scale factorial moment and intermittency are also introduced. Some debates indicate that intermittency is not a signal of the critical behavior. Finally, Nuclear Zipf's law has been proposed and it has been used to study the liquid gas phase transition of nuclei. At the point of phase transition, the cluster mass (charge) shows inversely to its rank, i.e. Zipf's law appears. Even though the criterion is still phenomenological, it is simple and practicable tool to diagnose the nuclear liquid gas phase transition in experiments and theories. The 4π multifragmentation data of heavy ion collision at Texas A&M University and GANIL as well as the CERN emulsion/plastic data have confirmed that the nuclear Zipf law is a valid probe for the liquid gas phase transition. The satisfaction of the Zipf law for the cluster distributions around the liquid gas phase transition illustrates that the clusters obey a particular rank ordering distribution rather than the equal-size fragment distribution as the spinodal instability predicts [84–88, 23]. It looks useful to distinguish the mechanism of the phase transition or fragment topological structure from the nuclear Zipf-type plots.

References

1. C.A. Ogilvie *et al.*, Phys. Rev. Lett. **67**, (1991) 1214; M.B. Tsang *et al.*, Phys. Rev. Lett. **71**, (1993) 1502; Y.G. Ma and W.Q. Shen, Phys. Rev. C **51**, (1995) 710.
2. M.E. Fisher, Physics (N.Y.) **3**, (1967) 255 .
3. S. Albergo, S. Costa, E. Costanzo, A. Rubbino, Nuovo Cimento **89A**, (1985) 1.
4. J. Pochodzalla et al., Phys. Rev. Lett. **75**, (1995) 1040.
5. Y. G. Ma et al., Phys. Lett. B **390**, (1997) 41.
6. J. B. Natowitz et al., Phys. Rev. C **65**, (2002) 034618.
7. J. B. Natowitz, K. Hagel, Y. G. Ma, M. Murray, L. Qin, R. Wada, and J. Wang, Phys. Rev. Lett. **89**, (2002) 212701.
8. W. Bauer, Phys. Rev. C **38**, (1988) 1297.
9. M. L. Gilkes et al., Phys. Rev. Lett. **73**, (1994) 1590.
10. M. D'Agostino et al., Nucl. Phys. A **650**, (1999) 329.
11. J. B. Elliott et al., Phys. Rev. C **55**, (1997) 1319.
12. J. B. Elliott et al., Phys. Rev. C **49**, (1994) 3185.
13. M. Kleine Berkenbusch, W. Bauer, K. Dillman, S. Pratt, L. Beaulieu, K. Kwiatkowski, T. Lefort, W.-c. Hsi, V. E. Viola, S. J. Yennello, R. G. Korteling, and H. Breuer, Phys. Rev. Lett. **88**, (2002) 022701.
14. Y. G. Ma et al. (NIMROD Collaboration), Phys. Rev. C **69**, 031604(R) (2004); Phys. Rev. C **71**, (2005) 054606.
15. J. Richert and P. Wagner, Phys. Rep. **350**, (2001) 1.
16. S. Das Gupta, A. Z. Mekjian, M. B. Tsang, Adv. Nucl. Phys. **26** , (2001) 89.
17. A. Bonasera, M. Bruno, C. O. Dorso, P. F. Mastinu, Riv. Del Nuovo. Cim. **23**,(2000) 1.
18. Ph. Chomaz, Procedings of the INPC 2001 Conference, Berkeley, Ca., July 2001.
19. L. G. Moretto, J. B. Elliott, L. Phair, G. J. Wozniak, C. M. Mader, and A. Chappars, Procedings of the INPC 2001 Conference, Berkeley, Ca., July 2001.
20. A. Kelic, J. B. Natowitz, K. H. Schmidt, Contribution to this book.
21. V. Viola, R. Bougault, Contribution to this book.
22. J. Elliott, K. A. Bugauev, L. G.Moretto, L.Phair, Contribution to this book.
23. B. Borderie, P. Desesquelles, Contribution to this book.
24. F. Gulminelli, M. DAgostino, Contribution to this book.
25. O. Lopez, M.F.Rivet, Contribution to this book.
26. X. Campi, J. Phys. A 19, L 917 (1986).
27. X. Campi, Phys. Lett. **B208**, (1988) 351.
28. W. Bauer et al., Phys. Lett. 150 B, 53 (1985).
29. W. Bauer et al., Nucl. Phys. A 452, 699 (1986).
30. D. Stauffer, *Introduction to Percolation Theory*, Taylor and Francis, London, 1985.
31. H. R. Jaqaman and D. H. E. Gross, Nucl. Phys. A **524**, (1991) 321.
32. N. Tan et al., Phys. Rev. B **29**, (1984) 6354.
33. B. K. Srivastava et al., Phys. Rev. C **65**, (2002) 054617.
34. J. A. Hauger et al., Phys. Rev. C **57**, (1998) 764.
35. J. A. Hauger et al., Phys. Rev. C **62**, (2000) 024616.
36. D. Cussol et al., Nucl. Phys. A **561**, (1993) 298.
37. J. Lauret et al., Phys. Rev. C **62**, (1998) R1051.
38. X. Campi and H. Krivine, Nucl. Phys. A **545**, (1992) 161c.
39. X. Campi and H. Krivine, Z. Phys. A **344**, (1992) 81.
40. J Péter et al., Nucl. Phys. A **593**,(1995) 95.
41. J. C. Steckmeyer et al., Phys. Rev. Lett. **76**, (1996) 4895.
42. X. Campi and H. Krivine, Nucl. Phys. A **589**, 505 (1995).
43. J. B. Elliott et al., Phys. Rev. C **67**, 024609 (2003).
44. Y. G. Ma et al., Nucl. Phys. A **749**, (2005) 106c.
45. C. O. Dorso, V. C. Latora, and A. Bonasera, Phys. Rev. C **60**, (1999) 034606.
46. Y. G. Ma, J. Phys. G **27**, (2001) 2455.
47. A. Bialas, R. Peschanski, Nucl. Phys. B **273**, 703 (1986).
48. M. Ploszajczak and A. Tucholski, Phys. Rev. Lett. **65**, 1539 (1999).
49. L. Phair et al., Phys. Lett. B **291**, 7 (1992).
50. B. Elatteri, J. Richert, P. Wagner, Phys. Rev. Lett. **69**, 45 (1992); ibid, Nucl. Phys. A **560**, 603 (1993).
51. H. W. Barz et al., Phys. Rev. C **45**, R2541 (1992).
52. V. Latora, M. Belkacem, A. Bonesera, Phys. Rev. Lett. **73**, 1765 (1994); M. Belkacem, V. Latora, A. Bonasera, Phys. Rev. C **52**, 271 (1995).
53. P. F. Mastinu et al., Phys. Rev. Lett. **76**, (1996) 2646.
54. Y. G. Ma, unpublished.
55. Y. G. Ma, Phys. Rev. Lett. **83**, (1999)3619.
56. Y. G. Ma, Eur. Phys. J. A **6**, (1999) 367.
57. G.K. Zipf, *Human Behavior and the Principle of Least Effort*, Addisson-Wesley Press, Cambridge, MA, 1949.
58. D. L. Turcotte, Rep. Prog. Phys. **62**,(1999) 1377.
59. M. Watanabe, Phys. Rev. E **53**, (1996) 4187.
60. T.D. Lee and C.N. Yang, Phys. Rev. **87**, (1952) 410.

61. T.S. Biro *et al.*, Nucl. Phys. A **459**, (1986) 692; S.K. Samaddar and J. Richert, Phys. Lett. B **218**, (1989) 381; Z. Phys. A **332**, (1989) 443; J.M. Carmona *et al.*, Nucl. Phys. A **643**, (1998) 115.
62. X. Campi and H. Krivine, Nucl. Phys. A **620**, (1997) 46.
63. J. Pan and S. Das Gupta, Phys. Rev. C **53**, (1996) 1319.
64. W.F.J. Müller, Phys. Rev. C **56**, (1997) 2873.
65. J. Pan and S. Das Gupta, Phys. Lett. B **344**, (1995) 29; Phys. Rev. C **51**, (1995) 1384; Phys. Rev. Lett. **80**, (1998) 1182; S. Das Gupta *et al.*, Nucl. Phys. A **621**, (1997) 897.
66. J. Pan and S. Das Gupta, Phys. Rev. C **57**, (1998) 1839.
67. F. Gullminelli and P. Chomaz, Phys. Rev. Lett. **82**, (1999) 1402.
68. Y.G. Ma et al., Phys. Rev. **C60**, (1999) 024607.
69. S. Ray *et al.*, Phys. Lett. B **392**, (1997) 7.
70. A. Coniglio and E. Klein, J. Phys. A **13**, (1980 2775).
71. L. Beaulieu et al., Phys. Rev. **C54**, (1996) R973.
72. Y.G. Ma et al., Euro. Phys. J. **A4**, (1999) 217.
73. N. Le Neindre, Talk at International Workshop on Multifragmentation (IWM2005), Nov. 28 - Dec. 1, 2005, Catania, Italy.
74. A. Dabrowska, M. Szarska, A. Trzupek, W. Wolter, B. Bosiek, Acta Phys. Pol. B **32**, (2001) 3099.
75. A. Dabrowska, M. Szarska, A. Trzupek, W. Wolter, B. Bosiek, Acta Phys. Pol. B **35**, (2004) 2109.
76. X. Campi and H. Krivine, Phys. Rev. C **72**, (2005) 057602.
77. W. Bauer, B. Alleman, S. Pratt, nucl-th/0512021.
78. S. Redner, Eur. Phys. J. B **4**, (1998) 131.
79. X. Campi, H. Krine, N. Sator, Physica A **296**, (2001) 24.
80. N. Sator, Phys. Rep. **376**, (2003) 1.
81. B. Mandelbrot, *An informational theory of the statistical structure of language*, in *Communication Theory*, ed. W. Jackson (Betterworths) 1953.
82. B. Mandelbrot, *The Fractal Geometry of Nature* (Freeman) 1982.
83. Ph. Chomaz, F. Gulminelli and V. Duflot, Phys. Rev. E **64**, (2001) 046114.
84. G. F. Bertsch and P. J. Siemens, Phys. Lett. **126B**, (1983) 9.
85. L. G. Moretto et al., Phys. Rev. Lett. **77**, (1996) 2634.
86. L. Beaulieu et al., Phys. Rev. Lett. **84**, (2000) 5971.
87. M. Colonna et al., Phys. Rev. Lett. **88**, (2002) 122701.
88. B. Borderie et al., Phys. Rev. Lett. **86**, (2001) 003252.